Mineralogy and Petrology
https://doi.org/10.1007/s00710-024-00869-y

RESEARCH

# Karlleuite $Ca_2MnO_4$ – a first mineral with the Ruddlesden-Popper type structure from Bellerberg volcano, Germany

**Juroszek Rafał[1] · Krüger Biljana[2] · Cametti Georgia[3] · Ternes Bernd[4] · Blaß Günter[5]**

Received: 11 June 2024 / Accepted: 29 July 2024


**Abstract**
Karlleuite, ideally $Ca_2MnO_4$, is a newly approved accessory mineral found in the xenolith sample within the basaltic lava from the Caspar quarry, Bellerberg volcano, Eifel, Germany. It usually occurs as thin tabular/plate crystals, which range from 40 to 80 μm in diameter, and is associated with other members of the perovskite supergroup such as srebrodolskite, brownmillerite, sharyginite, perovskite, and lakargiite distributed within rock-forming minerals represented by reinhardbraunsite, fluorellestadite, fluorapatite, larnite, gehlenite, and several hydrated Ca aluminosilicates. Karlleuite crystals are brown with sub-metallic lustre, a light brown streak, and a good cleavage along (001). It is non-fluorescent, brittle and has an uneven fracture, a Mohs hardness of 3.5 and calculated density $D_x$ = 3.79 g/cm$^3$. The empirical formula of the holotype karlleuite calculated based on O = 4 atoms per formula is $(Ca_{1.97}Ce^{3+}_{0.06})_{2.03}(Mn^{4+}_{0.39}Ti_{0.36}Fe^{3+}_{0.19}Al_{0.09})_{1.03}O_4$, which shows that it is a multicomponent phase characterised by various substituents at the octahedral site. Karlleuite is tetragonal *I*4/*mmm* (no. 139), with $a = 3.7683(2)$ Å, $c = 11.9893(8)$ Å, $V = 170.254(17)$ Å$^3$, and Z = 2. The calculated strongest lines in the X-ray powder diffraction pattern are [d in Å (I) hkl]: 5.995 (43), 2.742 (100), 2.665 (91), 2.023 (25), 1.998 (28), 1.884 (61), 1.553 (38), 1.371 (24). The new mineral is the first natural phase which exhibits a first order of Ruddlesden-Popper type structure, which indicates a modular nature and consists of Ca(Mn, Ti, Fe, Al)$O_3$ perovskite layers, packed between CaO rock-salt layers arranged along the *c*-axis. Raman spectroscopy supports the interpretation of the chemical and structural data. Mineral association, structural data, as well as the study of the synthetic Ca-Mn-O system suggest that karlleuite could form under high-temperature conditions, above 1000˚C.

**Keywords** Karlleuite · New mineral · Ruddlesden-Popper type structure · Bellerberg volcano · Perovskite supergroup

## Introduction

Ruddlesden-Popper (RP) phases are usually represented by perovskite-like layered oxides with the general formula $A_{n+1}B_nX_{3n+1}$, or $AX(ABX_3)_n$ ($n = 1, 2, 3, \ldots, \infty$), where *A* is typically an alkali, alkaline-earth or rare-earth metal ion, *B* is a transition or post-transition metal ion, and *X* is usually oxygen, which can be partially replaced by other non-metallic elements such as N, S, and Cl (Sharma and Singh 1998; Lacotte et al. 2014; Yu et al. 2017; Ablitt et al. 2020; Nirala

Editorial handling: L. Bindi.

✉ Juroszek Rafał
rafal.juroszek@us.edu.pl

Krüger Biljana
biljana.krueger@uibk.ac.at

Cametti Georgia
georgia.cametti@unibe.ch

Ternes Bernd
ternes-mayen@web.de

Blaß Günter
nc-blaszgu@netcologne.de

[1] Institute of Earth Sciences, Faculty of Natural Sciences, University of Silesia, Będzińska 60, Sosnowiec 41-200, Poland

[2] Institute of Mineralogy and Petrography, University of Innsbruck, Innrain 52, Innsbruck 6020, Austria

[3] Institute of Geological Sciences, University of Bern, Bern 3012, Switzerland

[4] Bahnhofstr. 45, Mayen D-56727, Germany

[5] Merzbachstr. 6, Eschweiler D-52249, Germany

Published online: 27 August 2024

et al. 2020; Ding et al. 2021; Marcondes et al. 2021). The crystal structure of RP family phases is characterised by $n$ consecutive perovskite layers ($ABX_3$) alternating with rock-salt layers ($AX$) along the crystallographic $c$-axis direction, where $n$ represents the number of connected perovskite layers of corner-sharing $BX_6$ octahedra, and goes from $n=1$ in $A_2BX_4$ to infinity in the well-known perovskite phase $ABX_3$ (Ruddlesden and Popper 1957; Lee and Lee 2017; Yu et al. 2017; Xu et al. 2020). As $n$ increases from 1 to ∞, the perovskite structure evolves from the two-dimensional (2D) RP layered to the three-dimensional (3D) simple perovskite structure (Yu et al. 2017; Nirala et al. 2020). The RP phases are known to exhibit a range of versatile and functional physical and optical properties such as magnetoresistance, photoluminescence, catalytic activity, superconductivity, as well as wide applications as electronic and magnetic functional materials (e.g., Moritomo et al. 1996; Hirayama et al. 1998; Gebhardt et al. 1999; Bassat et al. 2004; Gao and Wang 2006; Stanulis et al. 2014; Lee and Lee 2017; Sahu et al. 2018; Suter et al. 2018; Ding et al. 2021).

Among the various Ruddlesden-Popper phases, the members with $n=1$ ($A_2BX_4$), in particular the calcium manganates $Ca_2MnO_4$, are the best known. Such phases adopt the $K_2NiF_4$ structure, corresponding to the stoichiometric compound crystalized in the primitive $I4/mmm$ space group (Ruddlesden and Popper 1957; Fawcett et al. 1998; Surace et al. 2014). Moreover, the $n=1$ RP oxides allow a wide range of oxygen stoichiometries, from oxygen-stoichiometric to oxygen-deficient and oxygen-excess, depending on the oxygen defects (Chihaoui et al. 2011a; Yang et al. 2019). Similar to other members of the RP family, the $Ca_2MnO_4$ perovskite exhibits various magnetic, dielectric, and thermoelectric properties (Tezuka et al. 1999; Matar et al. 2005; Chihaoui et al. 2011b, 2013; Baranovskiy and Amouyal 2016). Furthermore, its layered structure and non-toxic and readily available chemical constituents make it a promising material for new battery cathodes (Surace et al. 2014).

Karlleuite is a natural counterpart of the $Ca_2MnO_4$ phase and a new accessory mineral, which has been found in the xenolith sample within the basaltic lava from the Caspar quarry locality, Bellerberg volcano lava field, Eastern Eifel region, Germany. It is also the first layered perovskite mineral with a $n=1$ Ruddlesden-Popper type structure. The new mineral (IMA2023-102), proposed name and symbol (Kll) have been approved by the Commission on New Minerals, Nomenclature and Classification (CNMNC) of the International Mineralogical Association (IMA). The holotype specimen is deposited in the Natural History Museum Mainz, State Collection for Natural History Rhineland-Palatinate, Reichklarastrasse 10, 55,116 Mainz, Germany, with the catalogue number NHMMZ M 2023/2-LS. The name karlleuite is given in honour of Karl Leu (b. 1958) from Nachtsheim, Germany, who started collecting minerals in the Eifel volcanic region in 1981. Karl Leu is an amateur mineralogist, collector, and specialist in the mineralogy of the Eifel region in Germany. His contribution is related to the fact that the lists of minerals found at various outcrops in the Eifel area could be extended. Moreover, Karl Leu is the author of many publications and reports on minerals from this region.

The present contribution provides a detailed description of the new mineral karlleuite from the Caspar quarry locality, including chemical, optical, spectroscopic, and structural data, as well as its comparison with related synthetic counterparts. The origin of karlleuite and its relationship to nomenclature of the perovskite supergroup are also discussed.

## Occurrence and paragenesis

Karlleuite was identified in the xenolith sample from the active Caspar quarry, Bellerberg volcano, Germany (50°21'6" N, 7°14'2" E). This distinctive geological area is a part of Quaternary volcanic field in the Eastern Eifel, Mayen-Koblenz, Rhineland-Palatinate, Germany (Hentschel 1987; Mihajlovic et al. 2004). The holotype location is characterised by the occurrence of various thermally metamorphosed xenoliths embedded in the basaltic lava of tephrite-leucite composition (Hentschel 1987; Mihajlovic et al. 2004). The diversity of mineral assemblages, usually in the contact zone of xenolith and volcanic rock, is mainly attributed to high-temperature transformations and different protolith compositions (Hentschel 1987; Juroszek et al. 2018, 2022; Juroszek and Ternes 2022). It is proclaimed by the presence of a dozen rare and new minerals, already found and described from this locality (Abraham et al. 1983; Hamm and Hentschel 1983; Effenberger et al. 1998; Juroszek et al. 2024).

The xenolith specimen with karlleuite was collected by Bernd Ternes and Günter Blaβ in the area of the open quarry in 1980. The xenolith zone, in which the new mineral was discovered, is characterised by different colours related to the main rock-forming components: pink for reinhardbraunsite, bluish for minerals of fluorellestadite-fluorapatite series, brownish-grey for larnite and highly altered gehlenite, and white for several hydrated Ca aluminosilicates. The accessory minerals are represented by chlormayenite, srebrodolskite, brownmillerite, sharyginite, perovskite, and lakargiite. Besides Ca aluminosilicates, typical low-temperature minerals include hydrocalumite, calcite, periclase, and ettringite.

**Table 1** Crystal data, parameters for X-ray data collection and crystal-structure refinement details for karlleuite

| Crystal data | Karlleuite |
|---|---|
| Refined chemical formula | $Ca_2(Mn_{0.37}Ti_{0.34}Fe_{0.19}Al_{0.10})O_4$ |
| Crystal system, Space group | Tetragonal, *I*4/*mmm* |
| Cell parameters | $a = 3.7683(2)$ Å |
| | $c = 11.9893(8)$ Å |
| Volume (Å$^3$) | 170.254(17) |
| $Z$ | 2 |
| $D_{calc.}$ (g·cm$^{-3}$) | 3.79 |
| μ (mm$^{-1}$) | 6.045 |
| Crystal size (mm) | 0.028 × 0.025 × 0.016 |
| Data collection | |
| Diffractometer | XtaLAB Synergy R |
| Radiation type | Mo*K*α |
| λ (Å) | 0.71073 |
| Detector | HyPix-Arc 100 |
| Temperature (K) | 302 |
| θ range (°) | 3.4-35.02 |
| Index ranges | $-5 \le h \le 5$ |
| | $-5 \le k \le 5$ |
| | $-18 \le l \le 18$ |
| No. of measured reflections | 2470 |
| No. of unique reflections | 138 |
| Refinement of the structure | |
| No. of parameters | 12 |
| $R_{int}$ | 0.0436 |
| $R_1$ (obs.) / $R_1$ (all) | 0.0287 / 0.0411 |
| *$wR_2$(obs.) / $wR_2$ (all) | 0.1001 / 0.1026 |
| GOF (obs.) / GOF (all) | 3.3393 / 3.7155 |
| Δρ max / Δρ min [e Å$^{-3}$] | 1.11 / -0.77 |

## Materials and methods of investigation

Petrographic thin sections and polished fragments of studied xenolith specimen with karlleuite and associated minerals were examined using a Leica DM2700P optical microscope under both transmitted and reflected light. Subsequently, studies of rock samples, including semiquantitative chemical compositions of minerals and their textural relationships, were carried out using a Phenom XL scanning electron microscope equipped with an EDS (energy-dispersive X-ray spectroscopy) detector. The semiquantitative EDS analyses were performed using a high vacuum with a beam voltage of 15 kV and a working distance of 6 mm.

Electron probe microanalyses (EPMA) of karlleuite were performed using a Cameca SX100 instrument operated at 15 kV, with the sample current 15 nA, and spot size ~ 1 μm, with the following lines and standards: Ti*K*α – rutile; Mn*K*α – rhodonite; Al*K*α – orthoclase; Fe*K*α – $Fe_2O_3$; Ce*K*α – $CeP_5O_{14}$; Ca*K*α – diopside.

The Raman spectra of karlleuite (Fig. 3 a, b) were recorded using a WITec alpha 300R confocal Raman microscope equipped with an air-cooled 532 nm solid-state laser and a CCD (charge-coupled device) camera operated at -61 °C. The Raman scattered light was focused by an effective pinhole size of about 30 μm and a monochromator with a 600 mm$^{-1}$ grating, calibrated by a Raman scattering line of a silicon plate (520.7 cm$^{-1}$). The power of the laser at the sample position was 42 mW. Data acquisition was performed with an integration time of 10 s, accumulation of 15 scans and a resolution of 3 cm$^{-1}$. Spectra processing, such as baseline correction and smoothing, was performed using the Spectracalc GRAMS software package. The Raman bands were fitted using a Gauss-Lorentz cross-product function with the minimum number of component bands used for the fitting process.

Single-crystal X-ray studies of karlleuite were carried out on a four-circle XtaLAB Synergy R diffractometer equipped with a rotating anode and HyPix-Arc 100 detector. The measurement was performed under ambient conditions at 302 K, and the data were collected using Mo*K*α radiation (λ = 0.71073 Å). Data reduction and determination of unit-cell parameters were processed using CrystAlisPro software (Rigaku Oxford Diffraction, 2022). Crystal structure solution and refinement of karlleuite were performed using Superflip and Jana2020 programs (Petříček et al. 2023). Further details of the data collection and crystal-structure refinement are given in Table 1. In turn, atomic coordinates, occupancies, equivalent and anisotropic displacement parameters are listed in Tables 2 and 3.

**Table 2** Atom coordinates (*x*,*y*,*z*), equivalent displacement parameters (*Ueq*, Å$^2$), and site occupancies for karlleuite

| Site | Atom | x | y | z | $U_{eq}$ | Occupancy |
|---|---|---|---|---|---|---|
| *A* | Ca1 | 0.5 | 0.5 | 0.85479(12) | 0.0155(3) | 1 |
| *B*$^*$ | Mn2 | 0.5 | 0.5 | 0.5 | 0.0140(4) | 0.37 |
| | Ti2 | | | | | 0.34 |
| | Fe2 | | | | | 0.19 |
| | Al2 | | | | | 0.10 |
| | O1 | 0.5 | 0.5 | 0.6664(5) | 0.0328(16) | 1 |
| | O2 | 0 | 0.5 | 0.5 | 0.033(2) | 1 |

$^*B = (Mn^{4+}_{0.39}Ti_{0.36}Fe_{0.19}Al_{0.09})$

**Table 3** Anisotropic displacement parameters (Å$^2$) of karlleuite

| Site | Atom | $U^{11}$ | $U^{22}$ | $U^{33}$ | $U^{12}$ | $U^{13}$ | $U^{23}$ |
|---|---|---|---|---|---|---|---|
| *A* | Ca | 0.0173(5) | 0.0173(5) | 0.0119(7) | 0 | 0 | 0 |
| *B* | Mn2<br>Ti2<br>Fe2<br>Al2 | 0.0097(5) | 0.0097(5) | 0.0224(9) | 0 | 0 | 0 |
| | O1 | 0.042(3) | 0.042(3) | 0.014(3) | 0 | 0 | 0 |
| | O2 | 0.011(3) | 0.043(4) | 0.044(4) | 0 | 0 | 0 |

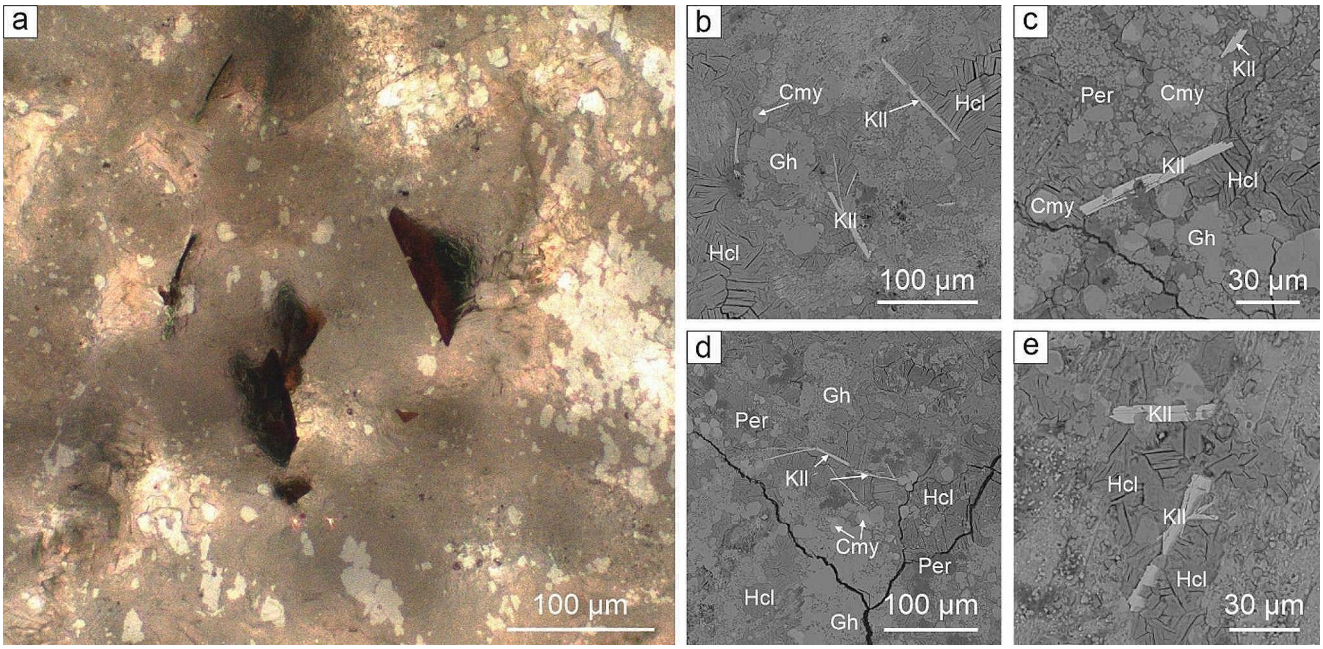


**Fig. 1** (**a**) Optical and (**b-e**) BSE (backscattered electrons) images of karlleuite and associated minerals within the holotype xenolith specimen. Abbreviations: Cmy – chlormayenite; Gh – gehlenite; Hcl – hydrocalumite; Kll – karlleuite; Per – periclase

## Results

### Physical and optical properties

Karlleuite is characterised by a brown colour with varying degrees of saturation from darker to lighter brown (Fig. 1a). The new mineral usually forms single thin tabular/plate crystals, which do not exceed 15 µm thickness, but range from 40 to 100 µm in length (Fig. 1b-e). Only in a few cases, the crystals reach more than 100 µm. Karlleuite is opaque in transmitted light, with a sub-metallic lustre, a light brown streak, and good cleavage parallel to (001). It is non-fluorescent, brittle and shows uneven fracture.

The bulk density was not directly measured due to the fracture and small crystal size. The calculated density 3.79 g/cm$^3$ was obtained from the empirical formula and unit-cell parameters refined from single-crystal data. Micro-hardness indentation was carried out using VHN (Vickers Hardness Number) for a load of 10 g, which gave a mean value of 254.6 kg/mm$^3$ (range from 240 to 266 kg/mm$^3$). This result corresponds to a hardness of 3.5 on the Mohs scale.

**Table 4** Reflectance values (%) for karlleuite

| $R_{max}/R_{min}$ | λ (nm) | $R_{max}/R_{min}$ | λ (nm) |
|---|---|---|---|
| 17.7/16.5 | 400 | 13.2/12.7 | 560 |
| 16.2/15.5 | 420 | 13.3/12.7 | 580 |
| 15.5/14.9 | 440 | 13.2/13.0 | 589 COM |
| 15.8/15.4 | 460 | 13.3/13.2 | 600 |
| 14.7/14.3 | 470 COM | 13.4/13.2 | 620 |
| 14.4/14.1 | 480 | 13.4/13.4 | 640 |
| 14.3/13.8 | 500 | 13.5/13.3 | 650 COM |
| 13.8/13.3 | 520 | 13.8/13.6 | 660 |
| 13.6/13.3 | 540 | 13.8/13.8 | 680 |
| 13.5/12.8 | 546 COM | 14.0/14.0 | 700 |

In reflected light, karlleuite is light grey and exhibits weak anisotropy under crossed polarisers. Quantitative reflectance measurements were performed in air relative to a SiC standard using a Leica FILMETRICS microscope-spectrophotometer, and the results are given in Table 4. The reflectance percentages for the four $R_{max}$ and $R_{min}$ COM

(Commission on Ore Mineralogy) wavelengths were: 14.7–14.3 (470 nm); 13.5–12.8 (546 nm); 13.2–13.0 (589 nm) and 13.5–13.3 (650 nm).

## Chemical composition

As karlleuite forms thin crystals, the measurement was challenging and some analyses with lower totals were omitted from the final calculation. The results of 10 spot analyses are given in Table 5. The high enrichment of $Ce_2O_3$ suggests the possibility of other REE (rare earth elements) in the chemical composition of karlleuite, so these were also measured. However, the obtained values were below the detection limits.

The empirical formula of karlleuite calculated on the basis of 4 O atoms per formula unit is $(Ca_{1.97}Ce^{3+}_{0.06})_{2.03}(Mn^{4+}_{0.39}Ti_{0.36}Fe^{3+}_{0.19}Al_{0.09})_{1.03}O_4$, which leads to the simplified formula $(Ca, Ce^{3+})_2(Mn^{4+},Ti, Fe^{3+},Al)O_4$. The ideal end-member formula $Ca_2MnO_4$ corresponds to 56.33% CaO and 43.67% $MnO_2$.

The holotype karlleuite is a multi-component phase, not an ideal end-member, as none of the distributed elements prevails over the *B* site. According to the IMA guidelines, the ideal formula was selected based on the dominant constituent rule (Hatert and Burke 2008). The calculated average composition indicated a significant Ti content (0.36 apfu) at the *B* site (Table 5). Similarly, the amount of trivalent cations Fe + Al (about 27%) present at this site, is relevant as well. The lowest and highest value (in wt%) of $MnO_2$ and $TiO_2$ do not show significant deviation from the average, indicating a relatively narrow compositional range (Table 5; Fig. 2). Nevertheless, some crystals showed an increased content of both $MnO_2$ and $TiO_2$. To confirm this observation, two additional analyses of karlleuite characterised by the highest content of $MnO_2$ (spot 16) and $TiO_2$ (spot 13) have been added to Table 5; Fig. 2. These data, not included in the calculation of the average composition due to the lower total amount, show the relationship between these two dominant constituents. An increase in the content of one leads to a decrease in the content of the other. Furthermore, these measurements confirm the existence of a solid solution between the two end-members $Ca_2MnO_4$-$Ca_2TiO_4$. The calculated empirical formula $(Ca_{2.03}Ce^{3+}_{0.03})_{2.06}(Ti_{0.44}Mn^{4+}_{0.31}Fe^{3+}_{0.18}Al_{0.10})_{1.03}O_4$ from analytical spot 13 shows the dominance of Ti at the *B* site and the possibility of recognition of a Ti-analogue of karlleuite within the holotype specimen.

## Raman spectroscopy

The Raman spectrum of karlleuite (Fig. 3a) is characterised by a strong and broad band at 559 $cm^{-1}$ with a shoulder,

**Table 5** Chemical composition (in wt%) for karlleuite

| Constituent | Mean ($n = 10$) | Range | SD | Spot 16* | Spot 13* |
|---|---|---|---|---|---|
| $TiO_2$ | 13.93 | 12.69–14.98 | 0.69 | 10.33 | 16.93 |
| $MnO_2$ | 16.53 | 15.98–16.64 | 0.20 | 18.17 | 13.15 |
| $Al_2O_3$ | 2.23 | 1.89–2.71 | 0.22 | 1.97 | 2.43 |
| $Fe_2O_3$ | 7.41 | 6.63–8.74 | 0.70 | 7.72 | 6.81 |
| $Ce_2O_3$ | 4.86 | 3.70–6.30 | 0.88 | 5.62 | 2.85 |
| CaO | 53.84 | 53.05–54.66 | 0.48 | 53.80 | 55.30 |
| Total | 98.80 | | | 97.61 | 97.47 |
| Calculated on 4 O | | | | | |
| $Ti^{4+}$ | 0.36 | | | 0.27 | 0.44 |
| $Mn^{4+}$ | 0.39 | | | 0.44 | 0.31 |
| $Al^{3+}$ | 0.09 | | | 0.08 | 0.10 |
| $Fe^{3+}$ | 0.19 | | | 0.20 | 0.18 |
| *Sum B* | 1.03 | | | 0.99 | 1.03 |
| $Ce^{3+}$ | 0.06 | | | 0.07 | 0.03 |
| $Ca^{2+}$ | 1.97 | | | 2.02 | 2.03 |
| *Sum A* | 2.03 | | | 2.09 | 2.06 |

*- not included in the calculation of the average composition; SD = 1σ = standard deviation

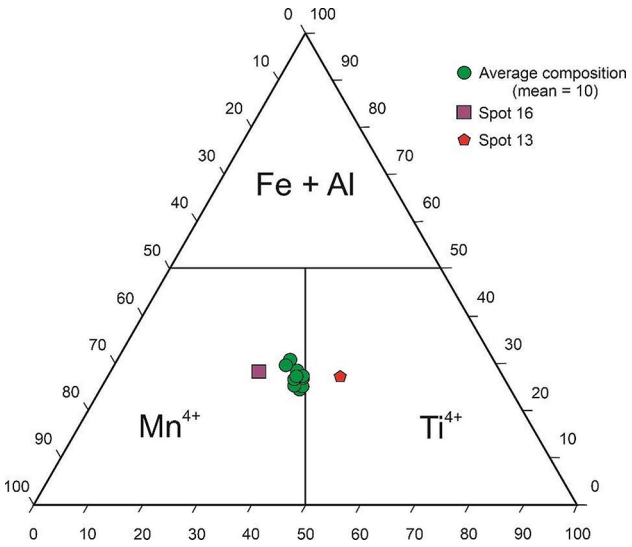


**Fig. 2** Ternary plot of the *B* site contents (apfu) of karlleuite according to the results obtained from EMP analyses

characterised by the relatively low intensity at 632 $cm^{-1}$. These bands are assigned to the symmetric stretching mode ($A_{1g}$) of the Mn-O-Mn vibration along the *c*-axis of the [$MnO_6$] octahedra. Two bands at 312 $cm^{-1}$ ($E_g$) and 505 $cm^{-1}$ ($B_{2g}$) are attributed to the sliding- and bending-type motions of the O atoms in the *ab* plane, respectively. The Raman band at 180 $cm^{-1}$ represents the rotational mode ($A_{1g}$) of [$MnO_6$] along the *c*-axis, similar to the Raman band at 286 $cm^{-1}$, corresponding to the rotation of Mn-octahedra. A band in the lower wavenumber region, ~110 $cm^{-1}$, is related to Ca-O stretching and lattice vibrations. The substitution by Ti at the octahedral site in the karlleuite structure is also evident from the Raman spectrum. The Raman band

at 207 $cm^{-1}$ is related to the rotational vibration of [$TiO_6$], whereas that at 765 $cm^{-1}$ is assigned to the breathing mode ($A_{1g}$) of [$TiO_6$] (Fig. 3a). In the Raman spectrum of karlleuite (Fig. 3b) performed in different orientations (rotation by 90° to the starting position) we noticed that there is a change in intensity between the Raman bands at 606 $cm^{-1}$ and 768 $cm^{-1}$ related to the symmetric stretching mode ($A_{1g}$) of the Mn-O-Mn vibration and the breathing mode ($A_{1g}$) of [$TiO_6$], respectively, compared to the spectrum presented in Fig. 3a. There is also an additional band at 1542 $cm^{-1}$, which is an overtone (Fig. 3b). The assignment of the karlleuite Raman bands is in good agreement with the previous spectroscopic studies carried out on the $Ca_2(Mn, Ti)O_4$ compound (Surace et al. 2014; Oka and Hayakawa 2022).

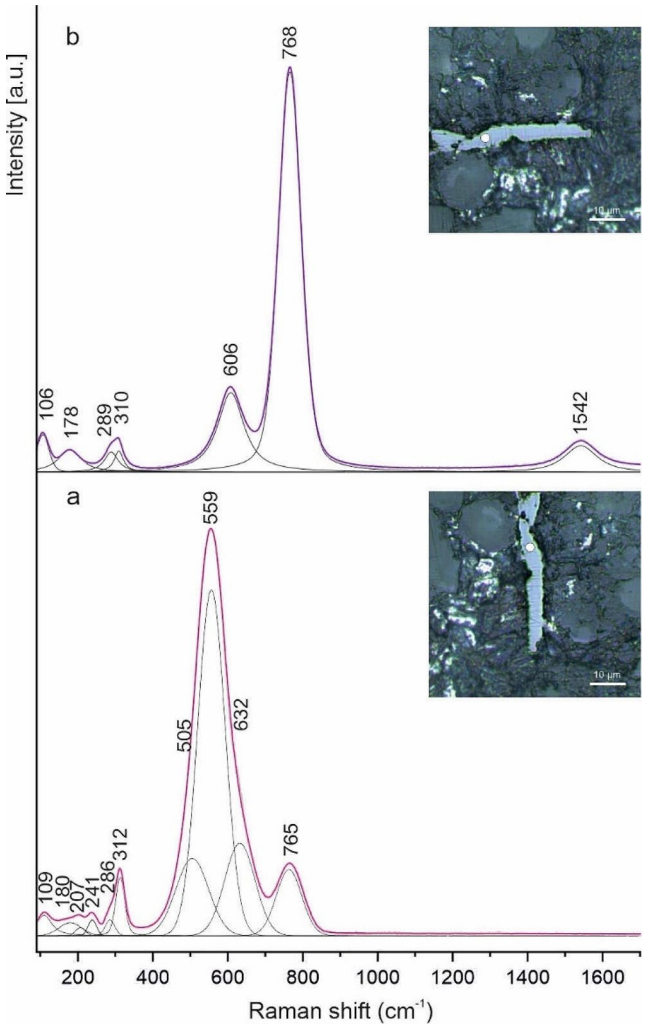


**Fig. 3** Raman spectra of karlleuite obtained at the two orientations relative to a polarised laser beam, along the elongation of crystal (**a**) and rotated by 90° (**b**). The analysis points are shown as white spots in the inset optical images

## X-ray crystallography

The crystal structure of karlleuite exhibits a Ruddlesden-Popper type structure characteristic of perovskite-like layered oxides. It is well known for synthetic phases, and karlleuite is the first natural compound to exhibit this structure type.

According to empirical formula $^{A}(Ca_{1.97}Ce^{3+}_{0.06})_{2.03}{}^{B}(Mn^{4+}_{0.39}Ti_{0.36}Fe^{3+}_{0.19}Al_{0.09})_{1.03}O_4$, the *A* site in karlleuite structure is occupied mainly by Ca with minor Ce, while the *B* site is occupied by a mixture of $Mn^{4+}$, Ti, Fe and Al. The structure refinement aimed at determining the accurate electron densities at the *A* and *B* positions. Using the Ca atom, the occupancy refinement of the *A* site converged to 1.001(8). Consequently, the Ce substitution was found to be insignificant, if present at all. Therefore, the occupation parameter of Ca was fixed to 1.

Occupancy refinement of the *B* site using Mn converged to 0.842(7). The total *B* site scattering is ~21.05(14) electrons per site. The average electron microprobe analysis for the same sample yielded $(Mn^{4+}_{0.39}Ti_{0.36}Fe^{3+}_{0.19}Al_{0.09})_{1.03}$, corresponding to ~23.8 electrons. The individual site occupancies of four elements could not be freely refined, as the Mn and Fe scattering curves are too similar for X-ray. Furthermore, with such a small number of unique reflections (109/138 reflections with $I > 3_{\sigma I}$), the number of parameters that can be meaningfully refined is very limited. Therefore, the site occupancy of all four elements at the *B* site was fixed according to the empirical formula and the anisotropic temperature parameters were refined (Tables 2 and 3).

The crystal structure of karlleuite display a modular nature and consists of $CaBO_3$ perovskite layers with *B* = (Mn, Ti, Fe, Al), packed between CaO rock-salt layers arranged along the *c*-axis (Fig. 4a, b). The Ca atoms, located at the boundary between the perovskite and rock salt layers, are coordinated by nine oxygen atoms. They have one short bond to the O1 site at 2.259(6) Å (along the *c*-axis), four bonds to O2 at 2.5653(10) Å, and four longer bonds to O1 equal to 2.6767(6) Å in the *ab*-plane (Fig. 4c). In perovskite layers, the octahedrally coordinated atom at the *B* site is bonded to four oxygen at O2 in the equatorial plane with bond lengths of 1.8842(2) Å, and two oxygen at O1 at the octahedra apex, with longer bond lengths equal to 1.994(5) Å (Fig. 4c).

Due to the small quantity and size of the karlleuite crystals, X-ray powder diffraction data were not collected. However, the data were calculated using the VESTA program from the results of the single-crystal structure refinement (Table 6; Fig. 5a) and the observed PXRD patterns were obtained by collapsing the single-crystal reflection into two dimensions using a Gandolfi-like screening procedure (Fig. 5b).

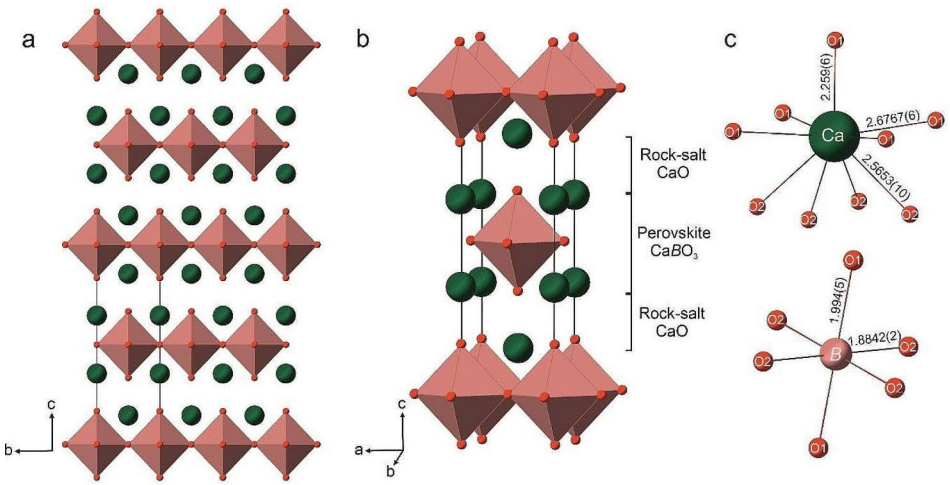


**Fig. 4** (**a**) The layered arrangement of atoms and octahedra along the *c*-axis in the crystal structure of karlleuite; (**b**) Schematic arrangement of Ruddlesden-Popper type-structure characteristic of karlleuite, comprising rock-salt (CaO) and perovskite layers $CaBO_3$ formed by Ca (green spheres) and $BO_6$ octahedra; (**c**) Selected bond lengths in the karlleuite structure

### BVS calculation and explanation

The adjustment of two different structural units, i.e., $CaBO_3$ and CaO, within the lattice causes strong anisotropic features in the $Ca_2BO_4$ structure. The structures of Ruddlesden-Popper type $n=1$, i.e., phase $A_2BO_4$, are known to exhibit bond valence sums (BVS) that deviate significantly from the theoretical one. This is due to the mismatch in size requirements of the perovskite and rock-salt type layers, leading to compression of the perovskite and elongation of the rock-salt type layers in the ab-plane (Brown 1992; Urusov and Orlov 1999).

For karlleuite structure, the BVS of Ca is 1.83 v.u. (valence units), indicating that Ca is slightly underbonded which is consistent with CaO with the rock-salt structure (*Fm*3*m*) and $CaMnO_3$ perovskite. In the case of the perovskite layers and octahedrally coordinated *B* site, the *B*-O bond lengths differ due to the Jahn-Teller distortion. A distortion where four bonds contract and two expand, termed $Q_3$, is typically observed in ordered perovskites (Kim et al. 2023). Distinguishing the substituents at the *B* site in the karlleuite structure, the BVS for each individual cation is: 3.857(11) v.u. for $Mn^{4+}$, 4.529(14) v.u. for $Ti^{4+}$, 3.964(12) v.u. for $Fe^{3+}$, and 2.917(8) v.u. for Al, clearly showing a mismatch of ionic radii and predicted *B*-O distances for all cations at this site (Table 7). Therefore, the obtained calculation shows that the O2 atom with an average BVS of 2.258 v.u. is overbonded, while O1 is underbonded with an average BVS of 1.568 v.u. (Table 7).

In CaO with a rock-salt structure (*Fm*3*m*), the O atom is coordinated by six Ca atoms, with bond lengths equal to 2.4048(1) Å, slightly larger than the predicted distance of 2.3735 Å. Therefore, in such structure type, oxygen atoms are usually slightly underbonded (1.838 v.u.) In the Ruddlesden-Popper structure, the Jahn Teller effect, and an elongation of the octahedra in the perovskite layers along the *c*-axis, causes longer *B*-O1 1.994(5) Å and shorter O1-Ca 2.259(6) Å bonds (Fig. 4c). Elongation of the rock-salt layers in the ab-plane leads to four long Ca-O1 bonds of 2.6767(6) Å and a very low bond valence sum of the O1 atom (Table 7).

In addition, the Goldschmidt tolerance factor ($t$) for karlleuite, where $A$ – O and $B$ – O are the metal – oxygen bond lengths of the A and B site, respectively is $t = \frac{A-O}{\sqrt{2}(B-O)} = 0.95$. Following Goldschmidt (1926), the RP type $n=1$ can be formed when $0.85 < t < 1.05$. When $t$ is close to unity, cubic perovskites (*Pm*3*m*) are stable at ambient conditions, when $t$ is greater or less than unity, disordered perovskite structures are expected.

The global instability index (GII), a bond valence-based metric originally designed to evaluate the total bond strain in a crystal (Brown 1992), of karlleuite is 0.3 v.u. which is much higher than the empirical threshold of 0.2, above which the feasibility of a structure should be doubted. Nevertheless, the majority of experimentally observed structures have GII values above the 0.2 v.u. threshold (Miller and Rondinelli 2023). Unlike $ABO_3$ oxides, which are generally known as oxygen-deficient perovskites because oxygen vacancies are their dominant anion defect, RP oxides can be both oxygen-deficient and oxygen-rich, depending on the majority of oxygen defects. However, in karlleuite structure, where the O1 and O2 atoms are fully occupied, we did not find evidence of these defects.

## Discussion

### $Ca_2MnO_4$ space group consideration

Synthetic, polycrystalline $Ca_2MnO_4$ was solved by Ruddlesden and Popper (1957) in the tetragonal *I*4/*mmm* space group with the following lattice parameters $a=3.67$ Å and $c=12.08$ Å, which match the here reported karlleuite

**Table 6** The calculated powder patterns of karlleuite

| d (Å) | I (%)* | h | k | l |
|---|---|---|---|---|
| 5.995 | 42.84 | 0 | 0 | 2 |
| 3.595 | 5.42 | 1 | 0 | 1 |
| 2.742 | 100.0 | 1 | 0 | 3 |
| 2.665 | 90.80 | 1 | 1 | 0 |
| 2.435 | 1.90 | 1 | 1 | 2 |
| 2.023 | 25.43 | 1 | 0 | 5 |
| 1.998 | 28.30 | 0 | 0 | 6 |
| 1.991 | 17.14 | 1 | 1 | 4 |
| 1.884 | 60.83 | 2 | 0 | 0 |
| 1.797 | 6.15 | 2 | 0 | 2 |
| 1.669 | 1.17 | 2 | 1 | 1 |
| 1.599 | 22.98 | 1 | 1 | 6 |
| 1.553 | 38.23 | 2 | 1 | 3 |
| 1.499 | 3.70 | 0 | 0 | 8 |
| 1.379 | 12.17 | 2 | 1 | 5 |
| 1.371 | 23.69 | 2 | 0 | 6 |
| 1.332 | 14.19 | 2 | 2 | 0 |
| 1.306 | 3.20 | 1 | 1 | 8 |
| 1.301 | 1.74 | 2 | 2 | 2 |
| 1.256 | 1.91 | 1 | 0 | 9 |
| 1.198 | 6.45 | 3 | 0 | 3 |
| 1.192 | 9.52 | 3 | 1 | 0 |
| 1.173 | 5.27 | 2 | 0 | 8 |
| 1.113 | 1.97 | 3 | 0 | 5 |
| 1.108 | 8.36 | 2 | 2 | 6 |
| 1.107 | 1.62 | 3 | 1 | 4 |
| 1.093 | 1.50 | 1 | 1 | 10 |
| 1.047 | 4.94 | 1 | 0 | 11 |
| 1.045 | 2.16 | 2 | 1 | 9 |
| 1.023 | 6.31 | 3 | 1 | 6 |
| 1.011 | 6.50 | 3 | 2 | 3 |
| 0.996 | 2.44 | 2 | 2 | 8 |
| 0.958 | 1.97 | 3 | 2 | 5 |
| 0.942 | 2.51 | 4 | 0 | 0 |
| 0.933 | 1.76 | 3 | 1 | 8 |
| 0.915 | 5.01 | 2 | 1 | 11 |
| 0.891 | 4.10 | 4 | 1 | 3 |
| 0.888 | 1.14 | 3 | 3 | 0 |
| 0.854 | 1.29 | 4 | 1 | 5 |
| 0.852 | 2.01 | 4 | 0 | 6 |
| 0.843 | 2.67 | 4 | 2 | 0 |
| 0.823 | 1.33 | 3 | 0 | 11 |
| 0.815 | 1.03 | 1 | 1 | 14 |
| 0.780 | 1.12 | 2 | 0 | 14 |
| 0.776 | 2.30 | 4 | 2 | 6 |
| 0.754 | 1.64 | 3 | 2 | 11 |
| 0.741 | 1.50 | 4 | 3 | 3 |
| 0.700 | 1.12 | 4 | 1 | 11 |

*Lines with relative intensities below 1% are omitted

structure. However, $Ca_2MnO_4$ phase can also crystalize in the tetragonal space group $I4_1/acd$ with lattice constants $a = 5.183(1)$ Å and $c = 24.117(4)$ Å, a super-cell ($a = \sqrt{2}a'$, $c = 2c'$) of the $I4/mmm$ unit cell, as reported by Leonowicz et al. (1985) and later confirmed by others (Takahashi and Kamegashira 1993; Fawcett et al. 1998; Taguchi 2001; Autret et al. 2004). Further investigations were performed also for Bi-, La-, Y-, and Dy-doped $Ca_2MnO_4$ (Kawashima et al. 2009; Azulay et al. 2020; Bregiroux et al. 2021). The doping of the *A* site by trivalent cations causes the electron excess, which is balanced by the reduction of an equivalent amount of $Mn^{4+}$ to $Mn^{3+}$ at the *B* site (Azulay et al. 2020; Bregiroux et al. 2021).

The difference between the tetragonal $I4/mmm$ and $I4_1/acd$ superstructures corresponds to the rotation of $MnO_6$ octahedra in opposite directions around the *c*-axis between two successive perovskite layers, and the rotation decreases with increasing temperature (Takahashi and Kamegashira 1993). The recent study confirms the occurrence of two tetragonal space groups for $Ca_2MnO_4$, wherein second order structural phase transition from $I4_1/acd$ to $I4/mmm$ is attained around 1050 K (Rocha-Rodrigues et al. 2020).

With this in mind, the ideal Ruddlesden-Popper type structure with $I4/mmm$ space group and *c* unit-cell parameter around 12 Å was finally determined for karlleuite (Fig. 6a). Naturally, there is no rotation or tilting of the octahedra in the consecutive perovskite layers (Fig. 6b). In comparison, an unselected and more complex structure with the $I4_1/acd$ space group is characterised by $MnO_6$ octahedra tilted about their *c*-axes, which are also slightly contra-rotated in the *ab* plane (Fig. 6d, e). This contra-rotation is related to each octahedron set placed on the first and third, as well as the second and fourth perovskite layers (Fig. 6e). Moreover, the rotation of the $MnO_6$ octahedra causes superlattice reflections and a doubling of the *c* parameter around 24 Å, which implies that the volume of the unit-cell with the $I4_1/acd$ space group is almost four times larger than that of the karlleuite $I4/mmm$ unit-cell (Fig. 6a, d). Superlattice reflexions can be a few magnitudes weaker than the main reflections. Therefore, sections of reciprocal space are constructed and extensively searched for any satellite reflections that can indicate possible superstructure. Still, no additional reflections were found. Furthermore, the phase transition between the two structures affects the Mn-O bond lengths together with the decrease of the Mn-O2-Mn angles between corner-connected octahedra from 180° in the $I4/mmm$ (Fig. 6c) to 161.6° in $I4_1/acd$ unit-cell (Fig. 6f; Leonowicz et al. 1985).

Considering that diffraction experiment was performed with powerful X-ray source (rotation anode) using the newest generation of hybrid pixel detector with excellent dynamic range, we are fairly sure that karlleuite exhibits undistorted $I4/mmm$ structure, as the most of the oxides with RP $n = 1$ structures (Balachandran et al. 2014).

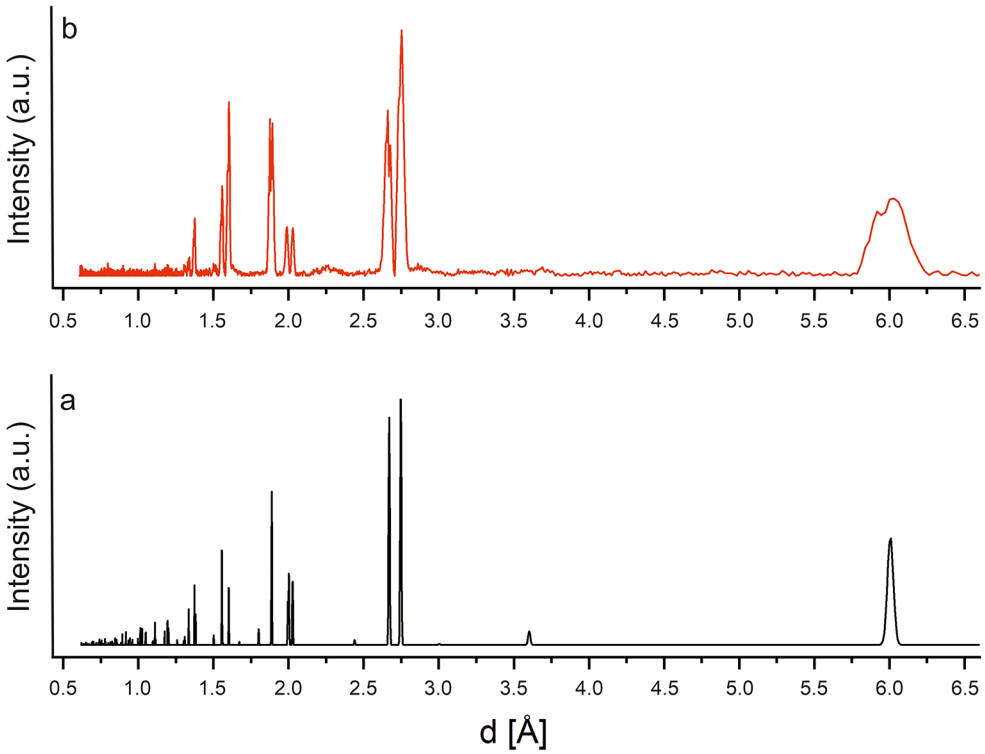


**Fig. 5** (**a**) X-ray powder diffraction data calculated from the results of the single-crystal structure refinement; (**b**) An observed PXRD obtained by collapsing the single-crystal reflections into two dimensions using Gandolfi-like screening procedure powder Graph(1.2.1) in CrysAlisPro software, applying using baseline correction and smooth filter. Both diagrams are calculated using λ = 0.71073 Å

**Table 7** Selected interatomic distances (Å) and BVS of the karlleuite structure

| Site 1 | Site 2 | Distance |
|---|---|---|
| *A* (Ca1) | O1 | 2.259(6) × 1 |
| | O1 | 2.6767(6) × 4 |
| | O2 | 2.5653(10) × 4 |
| | Mean | 2.5808 |
| | BVS | 1.83 |
| *B* (Mn2/Ti2/Fe2/Al2) | O1 | 1.994(5) × 2 |
| | O2 | 1.8842(2) × 4 |
| | Mean | 1.9208 |
| | [1]BVS *B* | 3.987 |
| O1 | Ca1 | 2.259(6) × 1 |
| | Ca1 | 2.6767(6) × 4 |
| | *B* | 1.994(5) |
| | Mean | 2.4933 |
| | [2]BVS (O1) | 1.404(8) – 1.602(11) |
| | average BVS (O1) | 1.568 |
| O2 | Ca1 | 2.5653(10) × 4 |
| | *B* | 1.8842(2) × 2 |
| | Mean | 2.3382 |
| | [2]BVS (O2) | 1.849(1) – 2.447(1) |
| | average BVS (O2) | 2.258 |

[1]BVS for *B* $[Mn_{0.37}Ti_{0.34}Fe_{0.19}Al_{0.10}]$; predicted distances: $Mn^{4+}$ – O = 1.9650 Å; $Ti^{4+}$–O = 2.0165 Å; $Fe^{3+}$–O = 2.0155 Å; $Al^{3+}$–O = 1.8765 Å; [2]BVS(O1) and BVS(O2) vary with *B* site cation. Bond valence parameters from Gagné and Hawthorne (2015)

## Genetic aspect of karlleuite formation and its relation to the perovskite supergroup

The formation of karlleuite is related to the Ca-rich pyrometamorphic rocks that occur as xenoliths in basaltic rocks in the Bellerberg volcanic region. Such rocks form under sanidine facies conditions, at temperatures above 1000˚C and low pressure ranging from a few kilobars to atmospheric conditions (Grapes 2010). Karlleuite is associated with $Fe^{3+}$-bearing minerals such as brownmillerite, srebrodolskite, and sharyginite, confirming high oxygen fugacity conditions during crystallization. The presence of these accessory minerals indicates their co-crystallization under similar conditions from compounds (fragments of Mn-Ti-Fe minerals) present in the sedimentary protolith. This suggests that karlleuite could be formed under high-temperature conditions. Moreover, investigations of the Ca-Mn-O system show that the $Ca_2MnO_4$ phase is stable over the wide temperature range between 700 and even 1550˚C (White et al. 2008). Furthermore, several studies on the synthetic $Ca_2MnO_4$ compound confirm its formation in the temperature range of 900–1200˚C (Fawcett et al. 1998; Autret et al. 2004; Kawashima et al. 2009; Chihaoui et al. 2011a), and the recently established temperature of $I4_1/acd \rightarrow I4/mmm$ phase transition around 1050 K (> 750˚C) fits into the stability field of this compound in the Ca-Mn-O system (Rocha-Rodrigues et al. 2020). The high-temperature origin of karlleuite could also be supported by its crystal structure with the *I*4/*mmm* space group. This hypothesis is reinforced

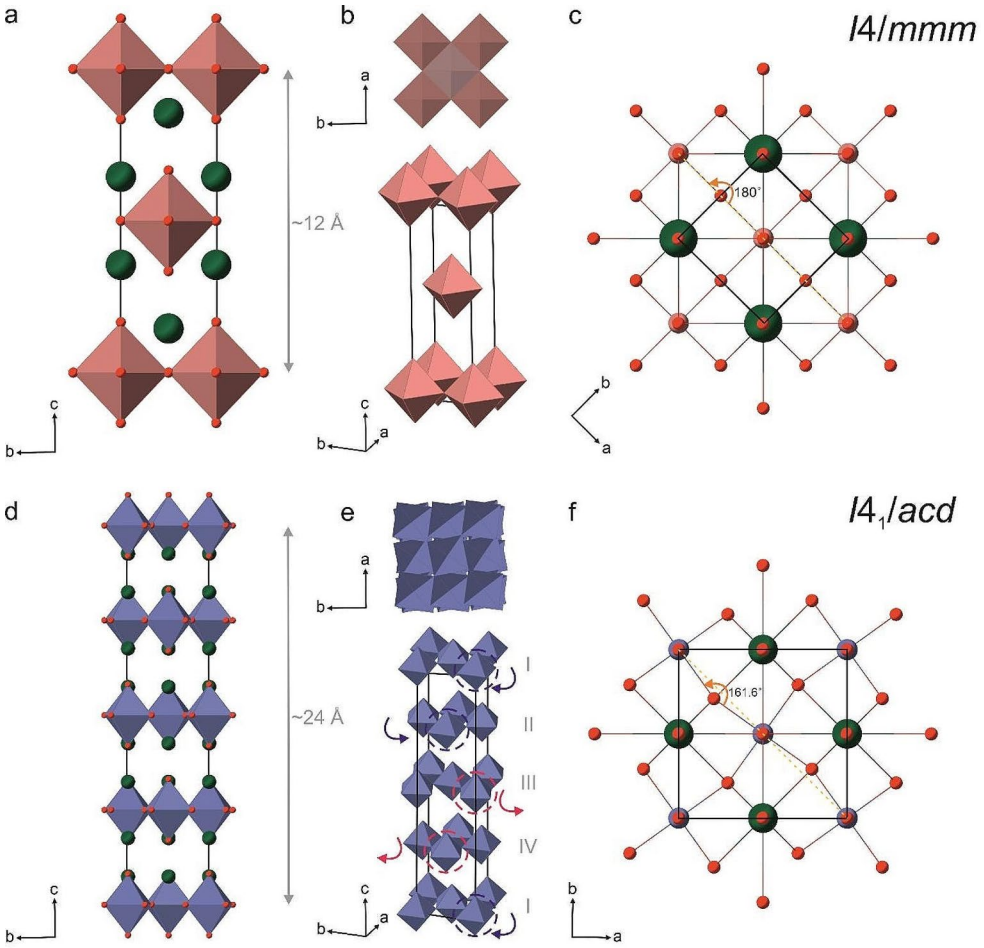


**Fig. 6** (**a**, **d**) Representation of the $Ca_2MnO_4$ structure in the *I*4/*mmm* (karlleuite) and supercell with $I4_1/acd$ space groups (after Leonowicz et al. 1985); (**b**, **e**) Representation of undistorted and distorted $MnO_6$ octahedra with characteristic rotation, view perpendicular and parallel to the *c*-axis; (**c**, **f**) Bonding scheme of the $Ca_2MnO_4$ structure with the relationship of the Mn-O2-Mn angle. Green and red spheres represent the Ca and O ions respectively, and Mn is shown as pink and purple octahedra (**a**-**b**, **d**-**e**) or spheres (**c**, **f**). The unit-cell is shown as a solid black line

by the fact that many oxides with the higher-symmetry crystallize under high-temperature conditions (Skinner 2003; Nirala et al. 2020).

According to the nomenclature of the perovskite supergroup (Mitchell et al. 2017), karlleuite does not fit into the classification of stoichiometric or non-stoichiometric perovskites. It can be included in the layered perovskites with the Ruddlesden-Popper type structure, derived from the simple aristotype $ABX_3$ structure, as presented in the hierarchical classification of synthetic compounds with the perovskite structure (Mitchell et al. 2017). Hitherto, no natural members with the Ruddlesden-Popper structure were previously known. As karlleuite is the first natural member characterised by this structure type, we propose to enrich the current classification with a potentially new, additional subgroup of minerals with the general formula $A_{n+1}B_nX_{3n+1}$, or $AX(ABX_3)_n$ ($n = 1$), according to the commonly used formula of synthetic compounds (Sharma and Singh 1998; Mitchell 2002; Lacotte et al. 2014). Karlleuite will be the first representative of this subgroup within the Ruddlesden-Popper type structure layered perovskites.

**Supplementary Information** The online version contains supplementary material available at https://doi.org/10.1007/s00710-024-00869-y.

**Acknowledgements** The investigation was partially supported by the National Science Center (NCN) of Poland Grant 2021/41/B/ST10/00130.

## References


Ablitt C, McCay H, Craddock S et al (2020) Tolerance Factor Control of Uniaxial Negative Thermal Expansion in a layered Perovskite. Chem Mater 32:605–610

Abraham K, Gebert W, Medenbach O et al (1983) Eifelite, $KNa_3Mg_4Si_{12}O_{30}$, a new mineral of the osumilite group with octahedral sodium. Contrib Mineral Petrol 82:252–258

Autret C, Martin C, Hervieu M et al (2004) Structural investigation of $Ca_2MnO_4$ by neutron powder diffraction and electron microscopy. J Solid St Chem 177:2044–2052

Azulay A, Wahabi M, Natanzon Y et al (2020) Enhanced Charge Transport in $Ca_2MnO_4$-Layered perovskites by point defect Engineering. ACS Appl Mater Interfaces 12:49768–49776

Balachandran PV, Puggioni D, Rondinelli JM (2014) Crystal-Chemistry guidelines for Noncentrosymmetric $A_2BO_4$ Ruddlesden – Popper Oxides. Inorg Chem 53:336–348

Baranovskiy A, Amouyal Y (2016) Structural stability of calcium-manganate based $CaO(CaMnO_3)m$ (m = 1, 2, 3, ∞) compounds for thermoelectric applications. J Alloys Compd 687:562–569

Bassat JM, Odier P, Villesuzanne A et al (2004) Anisotropic ionic transport properties in $La_2NiO_{4+\delta}$ single crystals. Solid State Ion 167:341–347

Bregiroux D, Bahezre A, Allani M et al (2021) Dysprosium doping of $Ca_2MnO_4$: Effect on crystal structure at room temperature and thermal behavior. Mater Chem Phys 267:124670

Brown ID (1992) Chemical and steric constraints in inorganic solids. Acta Cryst B 48:553–572

Chihaoui N, Bejar M, Dharhi E et al (2011a) Effect of the oxygen deficiency on the physical properties of $Ca_2MnO_{4-\delta}$ compounds. J Alloys Compd 8965–8969

Chihaoui N, Dhahri R, Bejar M et al (2011b) Electrical and dielectric properties of the $Ca_2MnO_{4-\delta}$ system. Solid State Commun 151:1331–1335

Chihaoui N, Bejar M, Dharhi E et al (2013) Dielectric relaxation of the $Ca_2MnO_{4-\delta}$ system. J Alloys Compd 577:483–S487

Ding P, Li W, Zhao H et al (2021) Review on Ruddlesden–Popper perovskites as cathode for solid oxide fuel cells. J Phys Mater 4:022002

Effenberger H, Giester G, Krause W, Bernhardt HJ (1998) Tschörtnerite, a copper-bearing zeolite from the Bellberg volcano, Eifel, Germany. Am Mineral 83:607–617

Fawcett ID, Sunstrom, Greenblatt M et al (1998) Structure, magnetism, and properties of Ruddlesden – Popper Calcium manganates prepared from citrate gels. Chem Mater 10:3643–3651

Gagné OC, Hawthorne FC (2015) Comprehensive derivation of bond-valence parameters for ion pairs involving oxygen. Acta Crystallogr B Struct Sci Cryst Eng Mater 71:562–578

Gao H, Wang Y (2006) Photoluminescence of $Eu^{3+}$ activated $Ba_2SnO_4$ under ultraviolet–vacuum ultraviolet excitation. J Mater Res 21:1857–1861

Gebhardt JR, Roy S, Ali N (1999) Colossal magnetoresistance in ce doped manganese oxides. J Appl Phys 85:5390–5392

Goldschmidt VM (1926) Die Gesetze Der Krystallochemie. Naturwissenschaften 14:477–485

Grapes R (2010) Pyrometamorphism. Springer, Berlin Heidelberg

Hamm HM, Hentschel G (1983) Reinhardbraunsite, $Ca_5(SiO_4)_2(OH,F)_2$, a new mineral - the natural equivalent of synthetic calcio-chondrodite. Neu Jb Mineral, 119–129

Hatert F, Burke EAJ (2008) The IMA-CNMNC dominant-constituent rule revisited and extended. Canad Mineral 46:717–728

Hentschel G (1987) Die Mineralien Der Eifelvulkane, 2nd edn. Weise, München, Germany

Hirayama T, Nakagawa M, Sumiyama A, Oda Y (1998) Superconducting properties in $La_2CuO_{4+\delta}$ with excess oxygen. Phys Rev B 58:5856–5861

Juroszek R, Ternes B (2022) Crystal chemistry and Raman spectroscopy study of bennesherite, $Ba_2Fe^{2+}Si_2O_7$, and rare accessory ba minerals from Caspar quarry, Bellerberg volcano, Germany. Mineral Mag 1–15

Juroszek R, Krüger H, Galuskina I et al (2018) Sharyginite, $Ca_3TiFe_2O_8$, a New Mineral from the Bellerberg Volcano. Ger Minerals 8:308

Juroszek R, Krüger B, Marciniak-Maliszewska B, Ternes B (2022) Minerals of the arctite supergroup from the Bellerberg volcano xenoliths, Germany. Mineral Mag 86:929–939

Juroszek R, Krüger B, Cametti G et al (2024) Karlleuite, IMA 2023 – 102, in: CNMNC Newsletter 78. Eur J Mineral 36

Kawashima F, Huang XY, Hayashi K et al (2009) Structure and high-temperature Thermoelectric properties of the n-Type layered Oxide $Ca_{2-x}Bi_{x-\delta}MnO_{4-\gamma}$. J Electron Mater 38

Kim WJ, Smeaton MA, Jia C et al (2023) Geometric frustration of Jahn-Teller order in the infinite-layer lattice. Nature 615:237–243

Lacotte M, David A, Pravarthana D et al (2014) Growth of $Ca_2MnO_4$ Ruddlesden-Popper structured thin films using combinatorial substrate epitaxy. J Appl Phys 116:245303

Lee D, Lee HN (2017) Controlling Oxygen mobility in Ruddlesden–Popper Oxides. Materials 10:368

Leonowicz ME, Poeppelmeier KR, Longo JM (1985) Structure determination of $Ca_2MnO_4$ and $Ca_2MnO_{3.5}$ by X-ray and neutron methods. J Solid St Chem 59:71–80

Marcondes ML, Santos SSM, Miranda IP et al (2021) On the stability of calcium and cadmium based Ruddlesden–Popper and double perovskite structures. J Mater Chem C 9:15074–15082

Matar SF, Subramanian MA, Weihrich R (2005) Ab initio investigation of the magnetic states of $Ca_2MnO_4$ and $Ca_2MnO_{3.5}$. Chem Phys 310:231–238

Mihajlovic T, Lengauer CL, Ntaflos T et al (2004) Two new minerals rondorfite, $Ca_8Mg[SiO_4]_4Cl_2$, and almarudite, $K(□,na)_2(Mn,Fe,mg)_2(be,Al)_3[Si_{12}O_{30}]$, and a study of iron-rich wadalite, $Ca_{12}[(Al_8Si_4Fe_2)O_{32}]Cl_6$, from the Bellerberg (Bellberg) volcano, Eifel, Germany. Neu Jb Mineral Abh 265–294

Miller KD, Rondinelli JM (2023) Testing the limits of the global instability index. APL Mater 11:101108

Mitchell RH (2002) Perovskites: modern and ancient. Almaz, Thunder Bay

Mitchell RH, Welch MD, Chakhmouradian AR (2017) Nomenclature of the perovskite supergroup: a hierarchical system of classification based on crystal structure and composition. Mineral Mag 81:411–461

Moritomo Y, Asamitsu A, Kuwahara H, Tokura Y (1996) Giant magnetoresistance of manganese oxides with a layered perovskite structure. Nature 380:141–144

Nirala G, Yadav D, Upadhyay S (2020) Ruddlesden-Popper phase $A_2BO_4$ oxides: recent studies on structure, electrical, dielectric, and optical properties. J Adv Ceram 9:129–148

Oka R, Hayakawa T (2022) Raman Spectroscopic Investigation and Electronic State Calculation for $Ca_2(mn,Ti)O_4$ black pigments with high Near-Infrared (NIR) reflectivity. Inorg Chem 61:6500–6507

Petříček V, Palatinus L, Plášil J, Dušek M (2023) Jana2020 – a new version of the crystallographic computing system Jana. Z Kristallogr – Cryst Mater 238:271–282

Rocha-Rodrigues P, Santos SSM, Oliveira GNP et al (2020) $Ca_2MnO_4$ structural path: following the negative thermal expansion at the local scale. Phys Rev B 102:104115

Ruddlesden SN, Popper P (1957) New compounds of the $K_2NiF_4$ type. Acta Cryst 10:538–539

Sahu M, Gupta SK, Jain D et al (2018) Solid state speciation of uranium and its local structure in $Sr_2CeO_4$ using photoluminescence spectroscopy. SAA 195:113–119

Sharma IB, Singh D (1998) Solid state chemistry of Ruddlesden-Popper type complex oxides. Bull Mater Sci 21:363–374

Skinner SJ (2003) Characterisation of $La_2NiO_{4+\delta}$ using in-situ high temperature neutron powder diffraction. Solid State Sci 5:419–426

Stanulis A, Katelnikovas A, Enseling D et al (2014) Luminescence properties of $Sm^{3+}$-doped alkaline earth Ortho-stannates. Opt Mater 36:1146–1152

Surace Y, Simões M, Eilertsen J et al (2014) Functionalization of $Ca_2MnO_{4-\delta}$ by controlled calcium extraction: activation for electrochemical Li intercalation. Solid State Ion 266:36–43

Suter A, Logvenov G, Boris AV et al (2018) Superconductivity drives magnetism in δ-doped $La_2CuO_4$. Phys Rev B 97:134522

Taguchi H (2001) Electrical property of $K_2NiF_4$-type $Ca_2(Mn_{1-x}Nb_x)O_4$. Mater Res Bull 36:1361–1367

Takahashi J, Kamegashira N (1993) X-ray structural study of calcium manganese oxide by rietveld analysis at high temperatures [$Ca_2MnO_{4.00}$]. Mater Res Bull 28:565–573

Tezuka K, Inamura M, Hinatsu Y (1999) Crystal Structures and Magnetic Properties of $Ca_{2+x}Sr_xMnO_4$. J Solid St Chem 145:705–710

Urusov VS, Orlov IP (1999) State-of-art and perspectives of the bond-Valence Model in Inorganic Crystal Chemistry. Crystallogr Rep 44:686–709

White BD, dos Santos CAM, Souza JA et al (2008) Crystal growth and characterization of Marokite $CaMn_2O_{4+\delta}$. J Cryst Growth 310:3325–3330

Xu X, Pan Y, Zhong Y et al (2020) Ruddlesden–Popper perovskites in electrocatalysis. Mater Horiz 7:2519–2565

Yang G, Jung W, Ahn S-J, Lee D (2019) Controlling the Oxygen Electrocatalysis on Perovskite and layered Oxide Thin films for solid oxide fuel cell cathodes. Appl Sci 9:1030

Yu Y, Zhang D, Yang P (2017) Ruddlesden-Popper Phase in two-Dimensional Inorganic Halide perovskites: a plausible model and the supporting observations. Nano Lett 17:5489–5494